Contents lists available at ScienceDirect

Bioactive Materials

Engineering self-healing adhesive hydrogels with antioxidant properties for intrauterine adhesion prevention

Luyao Feng [a,1], Liqun Wang [b,1], Yao Ma [a], Wanglin Duan [a], Sergio Martin-Saldaña [c], Ye Zhu [a], Xianpeng Zhang [a], Bin Zhu [a], Chaowei Li [a], Shibo Hu [a], Mingjie Bao [d], Ting Wang [d], Yuan Zhu [b,d,**], Fei Yang [e,f,***], Yazhong Bu [a,*]

[a] Institute of Medical Engineering, Department of Biophysics, School of Basic Medical Sciences, Health Science Center, Xi'an Jiaotong University, Xi'an, 710061, China
[b] Department of Reproductive Health, Jiangxi Maternal and Child Health Hospital, Nanchang, Jiangxi, 330006, China
[c] POLYMAT, Applied Chemistry Department, Faculty of Chemistry, University of the Basque Country UPV/EHU, Paseo Manuel de Lardizabal 3, 20018, Donostia-San Sebastián, Spain
[d] JXHC Key Laboratory of Fertility Preservation, Jiangxi Maternal and Child Health Hospital, Nanchang, Jiangxi, 330006, China
[e] School of Chemical Sciences, University of Chinese Academy of Sciences, Beijing, 100049, China
[f] Beijing National Laboratory for Molecular Sciences, State Key Laboratory of Polymer Physics & Chemistry, Institute of Chemistry, Chinese Academy of Sciences, Beijing, 100190, China

ARTICLE INFO

ABSTRACT

Intrauterine adhesion (IUA) is the fibrosis within the uterine cavity. It is the second most common cause of female infertility, significantly affecting women's physical and mental health. Current treatment strategies fail to provide a satisfactory therapeutic outcome for IUA patients, leaving an enormous challenge for reproductive science. A self-healing adhesive hydrogel with antioxidant properties will be highly helpful in IUA prevention. In this work, we prepare a series of self-healing hydrogels (P10G15, P10G20, and P10G25) with antioxidant and adhesive properties. Those hydrogels exhibit good self-healing properties and can adapt themselves to different structures. They possess good injectability and fit the shape of the human uterus. Moreover, the hydrogels exhibit good tissue adhesiveness, which is desirable for stable retention and therapeutic efficacy. The in vitro experiments using P10G20 show that the adhesive effectively scavenges ABTS+, DPPH, and hydroxyl radicals, rescuing cells from oxidative stress. In addition, P10G20 offers good hemocompatibility and in vitro and in vivo biocompatibility. Furthermore, P10G20 lowers down the in vivo oxidative stress and prevents IUA with less fibrotic tissue and better endometrial regeneration in the animal model. It can effectively downregulate fibrosis-related transforming growth factor beta 1 (TGF-β1) and vascular endothelial growth factor (VEGF). Altogether, these adhesives may be a good alternative for the clinical treatment of intrauterine adhesion.

1. Introduction

Intrauterine adhesion (IUA) is characterized by fibrosis within the uterine cavity due to damage or infection [1]. It leads to abdominal pain, oligomenorrhea, cyclical pelvic pain, and amenorrhea [2] and has become the second most common cause of female infertility [3–7]. Moreover, it shows an uprising incidence with the increase of intrauterine surgeries and induces serve influences on women's reproductive capacity and mental health [8]. The main therapeutic approach for IUA management in the clinic is hysteroscopy, which achieves an immediate reduction of internal adhesions. However, the recurrence rate is as high as 40%–62.5% [9,10]. Another common strategy is to introduce a physical barrier into the uterine cavity, including the placement of the balloon uterine stent (BUS), Foley catheters, silicon

sheets, or sodium hyaluronate injections [8,11]. However, solid devices like BUS and catheters cannot fit uterine cavities of different shapes and sizes, limiting their efficacy in marginal uterine positions [11]. Besides, the mechanical pressure induced by these devices may hinder tissue regeneration and cause inflammation [12]. Moreover, those devices are usually associated with a high risk of microbial infections [13]. Sodium hyaluronate can cover every cavity corner but has limited efficacy because of unstable retention. Thus, there is still a need for novel biomaterials aiming at effective IUA prevention.

Hydrogels are three-dimensional polymeric networks containing plenty of water [14]. They are widely explored in tissue engineering and regeneration due to their similarity to soft tissue [15]. Hydrogels are also studied in IUA prevention, and they should contain some desirable properties for better therapeutic effects [7,11,16]. Firstly, the hydrogels should be able to support the mechanical matrix of the uterine cavity and adjust themselves to different shapes of uterine cavities. This is vital because uterine cavities vary in shape and size under different pathological conditions [2]. Besides, the hydrogels must be injectable to avoid pain and discomfort to patients when passing through the narrow cervical orifice. Consequently, self-healing hydrogels are good candidates for meeting these requirements. They can be easily injected by passing through a narrow needle and recover their bulk strength after the injection because of their shear-thinning property [17], making them popular in non-invasive therapy [18]. On top of it, self-healing hydrogels can adapt themselves to different structures after application. This adaptability, with spatiotemporal and mechanical dynamics, may also regulate cellular behavior via stress relaxation, further contributing to the integration of biological signals to guide tissue regeneration [19]. However, there are few reports applying self-healing hydrogels in IUA prevention.

Bioactivity is also a desirable feature to prevent the formation of IUA and accelerate endometrial repair, considering the complex pathogenic mechanisms of IUA [2]. Briefly, IUA is a tissue fibrosis within the uterine cavity, and oxidative stress plays a vital role in tissue adhesion. It leads to vascular dysfunction and remodeling through oxidative damage, impairing vasodilatation and endothelial cell growth, stimulating endothelial cell migration, and activating adhesion molecules [20]. As a result, quenching the free radicals to modulate oxidative stress may be beneficial for IUA prevention [21–24]. However, the use of hydrogels with antioxidant properties in IUA prevention has not been explored yet.

Interface bonding is critical for functional hydrogels to reach their full potential in IUA therapy. On the one hand, proper integration can help maintain stability during the application. On the other hand, it can also ensure effective communication between biomaterials and tissue [25–27]. A healthy uterus of adult women secretes 3–4 g of endometrial mucus every 4 h [7]. Without suitable adhesion, the rapid turnover of mucus can easily result in the interfacial separation between the hydrogels and the uterine cavity tissue [28]. The separation will lead to poor retention of the functional hydrogels, decreasing their efficacy. Meanwhile, the gap between the hydrogels and the tissue surface will limit the biological functions of the functional hydrogels. Thus, hydrogels with adhesion properties will be advantageous in IUA prevention. Nevertheless, little consideration is given to introduce adhesion properties into hydrogels for better IUA therapeutic effects.

Hence, in this work, we have fabricated a series of self-healing adhesive hydrogels with inherent antioxidant properties for IUA prevention by using bi-polyethylene glycol N-hydroxysuccinimide active ester (Bi-PEG-SS) and gelatin. The hydrogels have tissue adhesion resulting from the reaction between Bi-PEG-SS and tissue proteins. The adhesive hydrogels exhibit great injectability, self-healing properties, and the ability to adapt to different structures. Besides, they demonstrate antioxidant properties against different free radicals and rescue cells from oxidative stress. Furthermore, in vivo experiments show that the adhesive hydrogels possess good biocompatibility. They effectively stop IUA with less fibrotic tissue and better endometrial regeneration through downregulating fibrosis-related cytokines, transforming growth factor

beta 1 (TGF-β1) and vascular endothelial growth factor (VEGF). These proposed adhesive hydrogels may offer a new alternative to IUA prevention in the clinic.

2. Methods

2.1. Synthesis of Bi-PEG-SS

The synthesis method of Bi-PEG-SS is the same as that reported in our previous article [29]. Briefly, two-arm polyethylene glycol with a molecular weight of 6000 Da and succinic anhydride were mixed in anhydrous dichloromethane under the catalysis of 4-dimethylaminopyridine overnight. The reaction mixture was centrifuged three times with 5% (w/w) NaCl solution to clean the impurities. Anhydrous magnesium sulfate was added to remove residual water. The reaction mixture was precipitated by petroleum ether, followed by roto evaporation, and vacuum drying. Then, a white blocky carboxyl-terminated polyethylene glycol was obtained. Later, carboxyl-terminated polyethylene glycol and N-hydroxysuccinimide (NHS) were mixed in anhydrous dichloromethane with the catalysis of 1-(3-dimethylaminopropyl)-3-ethylcarbodiimide hydrochloride (EDC) overnight. The above steps were repeated to obtain a white powder Bi-PEG-SS.

2.2. Preparation of injectable adhesive hydrogel

Different amounts of Bi-PEG-SS were dissolved in phosphate buffer solution (pH 4) for a final concentration of 10%, 15%, and 20% (w/v). In addition, different amounts of gelatin were dissolved in phosphate buffer solution (pH 9) at 55 °C for a final concentration of 15%, 20%, and 25% (w/v). A series of adhesive hydrogels were obtained by mixing different concentrations of Bi-PEG-SS and gelatin at the volume ratio of 1:1 to get P10G15, P10G20, P10G25, P15G25, P20G15, P20G20, and P20G25.

2.3. Self-healing ability test

The adhesive hydrogels were prepared and injected into the mold to form disc-shaped hydrogels (diameter 10 mm, height 6 mm). 5 min later, two discs were made for each hydrogel, one of which was stained with methylene blue. Then, the two disc-shaped hydrogels were crushed, and halves of each crushed hydrogels were mixed in disc molds. The molds were then sealed with parafilm and placed at 37 °C for 1 h after which the hydrogels were taken out for observation.

The adhesive hydrogels were prepared and injected into the mold to form strip-shaped hydrogels. 10 min later, two strips were made for each hydrogel, one of which was stained with methylene blue and the other was stained with rhodamine. Then, the two strips were cut into two halves. The halves from different strips were rejoined together and placed at 37 °C for 1 h. Finally, the repaired hydrogel in the mold was taken out for stretching test. Optical microscopy and scanning electron microscopy (SEM) were also used to observe the structure.

2.4. Rheology test

Dynamic rheological tests of the hydrogel samples (P10G15, P10G20, and P10G25) were carried out at 25 °C following previous report [30]. The rheological test was performed as follows: (1) adopting small shear strain (0.1%, 100 s), (2) increasing the shear strain until the gel fractures (1200%, 100 s), and (3) removing the strain at the same rate to the initial value ((0.1%, 100 s). The process was repeated twice.

2.5. Mechanical properties test

The adhesive hydrogels were prepared as cylindrical shape (diameter 8 mm, height 8 mm). 10 min later, the hydrogel was removed and cut into two pieces. Then, the two pieces were rejoined at the fracture site

and incubated at 37 °C for 1 h. Finally, the repaired hydrogels in the mold were taken out for compression test with universal tension machine.

For tensile strength, the adhesive hydrogels were prepared and injected into the mold to form strip-shaped hydrogels. After mixing for 10 min, the hydrogels were removed and cut into two pieces. Then, the two pieces were rejoined at the fracture and placed at 37 °C for 1 h. Finally, the repaired hydrogels in the mold were taken out for tensile test by universal tension machine.

2.6. In vitro swelling ratio and degradation time test

To test the swelling ratio of the adhesive hydrogels, 400 µL of those hydrogels were immersed into 5 mL of PBS solution and incubated at 37 °C. After 48 h of incubation, the hydrogels were taken out and gently dried by filter paper. The weights were measured, and the swelling ratios were calculated by the equation: $(W_t - W_0)/W_0 \times 100\%$. Where W_0 is the initial weight of each sample and W_t is the weight after 48 h of incubation.

To test the degradation profile, 400 µL of the adhesive hydrogels were immersed into 5 mL of PBS solution and incubated at 37 °C. After 1, 2, 3, 4, 5, 6, and 7 days of incubation, the hydrogels were removed and gently dried with filter paper. The weights were measured, and the degradation curve was recorded. (n = 3).

2.7. Adhesion strength test

Adhesive strength test was performed with porcine skin. The porcine skin was cut into a rectangle (length 25 mm, width 10 mm). P10G15, P10G20, and P10G25 (40 µL) were injected on one piece of skin. Then, the two skin pieces were overlapped and pressed for 1 min. Subsequently, the porcine skin was incubated at 37 °C for 0.5 h. Five replicate samples were made for each formulation. Finally, the adhesive strength was evaluated by an electronic universal testing machine (CMT1103, Zhuhai Sansi Test Equipment Co., Ltd, China).

2.8. Injectability and shape suitability test

P10G15, P10G20, and P10G25 were prepared and injected into different shapes of molds through long catheters with the inner diameter to be 1.5 mm. Then, the hydrogels were removed and crushed. Then, the crushed hydrogels pieces were mixed and placed into a mold of tree shape. Finally, the mold was incubated at 37 °C for 1 h after which the hydrogel was taken out for observation.

For the injection into the rat stomach, the stomach was removed from the Sprague Dawley rat and the gastric contents were rinsed. The hydrogel was injected into the stomach with a syringe through a catheter (1.5 mm). After 10 min, the rat's stomach was opened, and the hydrogel was taken out for observation. In the balloon group, one end of the stomach was ligated, and the balloon was inserted into the stomach from the other end. Then, the balloon was inflated to support the stomach.

2.9. Antioxidant properties assessment

2.9.1. ABTS$^+$ radical scavenging assay

ABTS$^+$ radical solution was prepared by mixing 25 mL of 7.4 mM ABTS$^+$ (2,2′-azino-bis (3-ethylbenzothiazolin-6-sulfonic acid) radical solution with 25 mL of 2.45 mM potassium persulfate solution which was then incubated in the dark environment for 12 h at 25 °C. 50 µL of ABTS$^+$ radical stock solution was added to 3 mL of water for dilution. Different masses of P10G20 (10, 30, and 50 mg) and ascorbic acid solutions (VC, 0.05 mg/mL, 150 µL) were added to the 3 mL of diluted ABTS$^+$ radical solutions, which were then incubated for 20 min at 25 °C in the dark. VC solution was used as the positive control. The absorbance at 734 nm was measured using a microplate reader. ABTS$^+$ radical scavenging activity was calculated according to the following equation:

ABTS$^+$ radical scavenging ratio (%) = $[(A_0 - A_1)/A_0] \times 100$, where A_0 is the absorbance of the control (0 mg), and A_1 is the absorbance of the sample (10, 30, and 50 mg) and VC (0.05 mg/mL, 150 µL) groups. The experiment was repeated three times for each concentration.

2.9.2. DPPH radical scavenging assay

DPPH (2, 2-diphenyl-1-trinitrohydrazyl) radical solution (0.1 mg/mL) was prepared by dissolving DPPH radical into the methanol. Different mass of P10G20 (40, 70, and 100 mg) and ascorbic VC (0.5 mg/mL, 50 µL) were added to 3 mL of DPPH radical solution. VC was used as the positive control. The mixed solution was incubated for 20 h at 25 °C in the dark. The absorbance of the mixed solution at 517 nm was measured using a microplate reader. DPPH radical scavenging activity was calculated according to the following equation: DPPH radical scavenging ratio (%) = $[(A_0 - A_1)/A_0] \times 100$, where A_0 is the absorbance of the control (0 mg), and A_1 is the absorbance of the sample (40, 70, and 100 mg) and VC (0.5 mg/mL, 50 µL) groups. The experiment was repeated three times at each concentration.

2.9.3. Hydroxyl radical scavenging assay

Hydroxyl radical was generated in a Fenton-type reaction [31]. A stock solution of hydroxyl radicals was prepared by mixing an equal volume of 9 mM salicylic acid ethanol solution, an aqueous solution of 9 mM ferrous sulfate, and an aqueous solution of 8.8 mM hydrogen peroxide. Dilution was performed by adding 1.5 mL of water to 1.5 mL of stock solution. P10G20 (10, 30, and 50 mg) and VC (2 mg/mL, 160 µL) were added to 3 mL of diluted hydroxyl radical solution. VC was used as the positive control. The mixed solution was incubated at 25 °C for 10 min in the dark before centrifugation (5000 r/min, 4 min). The absorbance at 510 nm was then measured using a microplate reader. Hydroxyl radical scavenging activity was calculated according to the following equation: Hydroxyl radical scavenging ratio (%) = $[(A_0 - A_1)/A_0] \times 100$, where A_0 is the absorbance of the control (0 mg), and A_1 is the absorbance of the sample (10, 30, and 50 mg) and VC (2 mg/mL, 160 µL). The experiment was repeated three times at each concentration.

2.9.4. Antioxidant experiments with cells

The ability to rescue cells from oxidative stress was evaluated with P10G20 over NIH 3T3 mouse fibroblasts. Firstly, NIH 3T3 mouse fibroblasts were seeded into 48-well plates (3000 cells per well) and cultured at 37 °C under 5% CO$_2$ to achieve the adhesion after the overnight incubation. Then, *tert*-butyl hydroperoxide (*t*BOOH, 100 µM) was added to the cells to induce oxidative stress. For the treatment group, P10G20 (20, 30, and 50 mg) were mixed with *t*BOOH for 20 min and then added into the cell culture medium. After 5 h, metabolic activity was determined by cell counting kit-8 (CCK8) and live/dead cell staining kit.

2.10. In vitro biocompatibility tests

The cytotoxicity of P10G20 was evaluated using NIH 3T3 mouse fibroblast with CCK8. Before tests, the raw materials and the hydrogels were sterilized under UV light for 30 min. Then, P10G20 (200 mg) was placed in fresh cell culture medium (10 mL) overnight (12 h) to obtain the leaching solution (1X). The leaching solution was then diluted using culture medium to be 10X, 100X, and 1000X. The P10G20 (1 g) was placed in fresh medium (10 mL) until it was completely degraded to obtain the degradation solution. Then, it was diluted into different concentrations (20 mg/mL, 2 mg/mL, 0.2 mg/mL, and 0.02 mg/mL). NIH 3T3 mouse fibroblasts were seeded in 96-well plates (3000 cells per well) and cultured at 37 °C, 5% CO$_2$. After the cells' adhesion, the cell culture medium was replaced with different concentrations of leaching contents and degradation solutions. After 24 and 48 h, 10% CCK8 was added into each well. The absorbance of the sample solution was detected with a microplate reader (SuperMax 3100, Shanghai Shanpu

Biotechnology Co., Ltd) at 450 nm. Metabolic activity above 70% was considered non-cytotoxic. Co-culture with P10G20 (5, 10, 20, and 50 mg) was performed in a 48-well cell culture plate (1×10^4 cells/well), and the rest steps are the same as above.

Furthermore, the cytotoxicity was evaluated using live/dead cell staining kit. As mentioned above, the cells were treated with the leaching content and degradation products, and co-cultured with P10G20. After 24 h and 48 h of incubation, the leaching content, degradation solution and P10G20 were removed and washed twice with PBS. Then live/dead cell staining was performed according to the instructions, and cell viability and adhesion were observed with an inverted fluorescence microscope.

2.11. In vitro hemolysis test

Fresh blood from Sprague Dawley rat (2 mL) was mixed with normal saline (20 mL), and the supernatant was discarded by centrifugation (1200 rpm, 15 min). After three times of centrifuging, the solutions were diluted to 2% (V/V) with normal saline. Different concentrations of P10G20 leaching content (0.5 mL) and erythrocyte suspension (0.5 mL) were mixed as experimental group (defined as W_1). Deionized water (0.5 mL) and saline (0.5 mL) were mixed with erythrocyte suspension (0.5 mL) as positive control (defined as W_0) and negative control (defined as W_2), respectively. All samples were placed at 37 °C for 1.5 h. After centrifuging the samples, the supernatant was pipetted into a 96-well plate to measure the samples absorbance, and the detection wavelength was 540 nm. Finally, the hemolysis rate calculation formula: hemolysis ratio (%) = $(W_1 - W_2)/(W_0 - W_2) \times 100$.

2.12. In vivo biocompatibility test

Sprague Dawley rats (female, weight of 190–250 g) were used in this experiment. After anesthesia, a small incision was made in the middle of the lower abdomen to expose the uterus. The left uterus of the rat was used as the experimental group (n = 3). A 5 mL syringe was used to poke a small hole just above the junction of the uterus, after which 300 μL of hydrogels were injected to fill the uterus. The right uterus was used as the blank control group without any treatment (n = 3). After the surgery, the abdominal wall was sutured layer by layer. At the chosen time, the rats were euthanized, and the uteri were observed and harvested for H&E and Masson staining. H&E staining was mainly used to observe uterine morphology, endometrial thickness and number of endometrial glands. Masson staining was used to analyze the area of endometrial fibrosis.

2.13. In vivo antiadhesion experiments

Sprague Dawley rats (female, weight of 190–250 g) were used in the antiadhesion experiments. The left uteri of all rats were divided into IUA model group (Saline group, n = 6) and P10G20 treatment group (P10G20 group, n = 6). The right uteri of all rats were used as the blank control group (healthy group, n = 12). After anesthesia, a small incision was made in the middle of the lower abdomen to expose the uterus. Then a scraping hook made of 26 G needle was inserted to scrape one side of the left endometrial tissue until hyperemia was visible to the naked eye. After that, a syringe with a small catheter (Inner diameter: 1 mm) was inserted into the uterine cavity. In Saline group, 300 μL saline solution was injected to rinse the uterus. In P10G20 group, 300 μL of hydrogel was injected to fill the uterine cavity. Uteri in healthy group were left untreated after exposure for 20 min. Finally, the abdominal cavity was closed layer by layer. 7 days post-surgery, the rats were euthanized, and uterine tissues were excised. After the observation, H&E and Masson staining were carried out to check the pathological changes.

2.14. In vivo antioxidant tests

The in vivo antioxidant properties were indicated by the H_2O_2 content with Ferric-xylenol orange (FOX1) assay described by Erel. et al. with slight modifications [32]. After 0.5, 1, 3, and 7 days of surgery (n = 3), the uterine tissue was excised. Then, the removed uterine tissue was weighed after being cleaned with normal saline, after which the tissue was put into normal saline at a concentration of 100 mg/mL to make tissue homogenate. After centrifugation (12000 r/min, 5 min), the supernatants were collected. 500 μL of the supernatants was mixed with 500 μL of FOX1 reaction solution and incubated at room temperature for 30 min. After centrifugation, the absorbance of the supernatants at 560 nm was measured, and the H_2O_2 content in uterine tissue was calculated according to the standard curve.

2.15. RNA extraction reverse transcription and quantitative real-time PCR (qRT-PCR)

The rats were euthanized at 1, 3, and 7 days after the surgery (n = 3), and uterine tissues were excised. After that, uterine tissues were snap-frozen in liquid nitrogen within 30 min, and the rest steps are the same as above. Total RNA was purified from frozen uterine specimens using RNAeasy™ Animal RNA Isolation Kit with Spin Column following the standard protocol (Beyotime Biotechnology). The purity and concentration of RNA were identified. Later, cDNA was obtained via the PrimerScriptRT Master Mix (Takara, Japan). qRT-PCR was conducted following the standard protocol (SYBR Green qPCR Mix, biosharp).

GAPDH was used as a normalization control when assessing relative gene expression. The relative expressions of the target genes were calculated using the $2^{-\Delta\Delta CT}$ method. The primer sequences of target genes are listed as below. TGF-β1-forward: 5′- GACCGCAA-CAACGCAATCTA-3′, TGF-β1-reverse: 5′- TTCCGTCTCCTTGGTTCAGC-3′, VEGF-forward: 5′- AGAAAGCCCATGAAGTGGTGA-3′, VEGF-reverse: 5′- GCTGGCTTTGGTGAGGTTTG-3′, GAPDH-forward: 5′- TTGTGCAGTGCCAGCCTC-3′, GAPDH-reverse: 5′- GATGGT-GATGGGTTTCCCGT-3′.

2.16. Statistical analysis

SPSS 26 was used for statistical calculations. Data were expressed as mean ± standard deviation (SD). In the statistical analysis for multiple comparisons, one-way analysis of variance (ANOVA) followed by Tukey and Dunnett post-hoc test was conducted. The statistical analysis between two data groups was determined with Student's t-test. A value of $p < 0.05$ was considered statistically significantly different (*$p < 0.05$, **$p < 0.01$, ***$p < 0.001$, and ****$p < 0.0001$).

3. Results and discussion

3.1. Preparation and characterization of self-healing hydrogels

The proposed adhesive hydrogels were fabricated by using Bi-PEG-SS and gelatin. When mixing Bi-PEG-SS (Fig. S1) and gelatin, Bi-PEG-SS started to crosslink with gelatin and form a gel. There are plenty of dynamic non-covalent bonds occurring in the polymeric network because of gelatin's structure, including electrostatic interactions and hydrogen bonds (Scheme 1) [33]. It was hypothesized that once broken, the non-covalent bonds broke first because of their weak bonding strength. When the interfaces were reconnected, the hydrogels self-healed because of the self-healing of those non-covalent bonds. To find the optimal ratio for later experiments, different concentrations of Bi-PEG-SS and gelatin were mixed at equal volumes to make a series of hydrogels, including P10G15, P10G20, P10G25, P15G25, P20G15, P20G20, and P20G25. Fig. 1a showed that they all became the gel state after mixing different concentrations of Bi-PEG-SS and gelatin. To further prove that the gelation did not result from the physical gelation
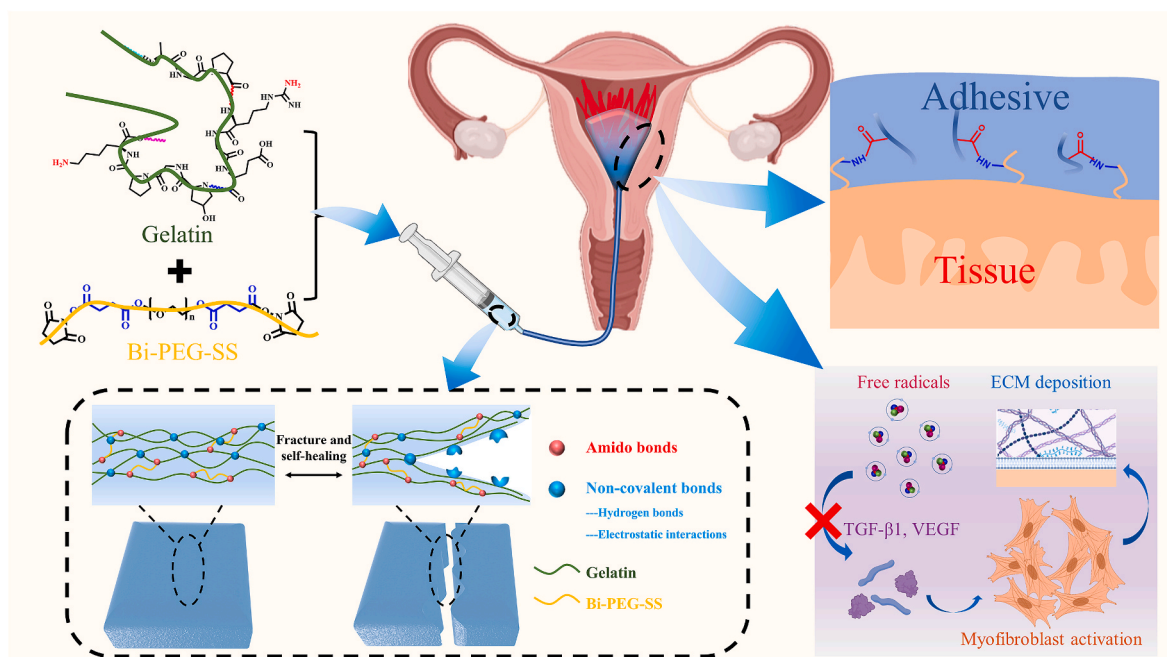
Scheme 1. Scheme showing engineering of a self-healing adhesive hydrogel with antioxidant properties for IUA prevention. The adhesive was fabricated by mixing Bi-PEG-SS and gelatin. The mixed adhesive hydrogels were injected into the injured uterine cavity, and adhesion was achieved by the ammonolysis reaction between amino groups from tissue and succinimidyl succinate (active ester) from the adhesive hydrogels. The self-healing properties of adhesive hydrogels were conferred by non-covalent bonds in the network, including hydrogen bonds and electrostatic interactions. Because of the inherent antioxidant properties, the adhesive hydrogels could reduce free radicals to down-regulate TGF-β1 and VEGF to modulate extracellular matrix (ECM) deposition and myofibroblast activation for IUA prevention.

of gelatin, a dissolution experiment was carried out using P10G20 as an example (Fig. S2). In addition to using gelatin as a control, the mixture of gelatin with polyethylene glycol (Bi-PEG-OH) was also used to show if the PEG chain would influence the gelation behavior. It was demonstrated that hydrogels, made of gelatin, and the mixture of gelatin and Bi-PEG-OH, dissolved at 37 °C in less than 1 h. At the same time, P10G20 kept stable, proving the chemical crosslinking between gelatin and Bi-PEG-SS. Fig. 1a also showed that after increasing the concentration of Bi-PEG-SS to 15 wt%, the gel showed semitransparency and non-transparency. We deduced that this happened due to the more significant polymer concentration that led to fast gelation, which occurred before the polymers could evenly distribute themselves. As a result, the transparency of these hydrogels was decreased because of the aggregated polymers. The uneven crosslinking would also impair the mechanical strength of the resulting hydrogels [34]. Hence, P10G15, P10G20, and P10G25 were used in later experiments.

P10G15 to P10G25 were shaped into disk molds (Fig. 1b). After gelation, they were crushed and re-put in the molds. The adhesive hydrogels were observed to self-heal to the disc shape at 37 °C after 1 h, showing that they possessed self-healing properties. Furthermore, two differently stained adhesive strips were cut into two pieces and rejoined together. After 1 h of incubation, the interface was obviously blurred, and the resulting new strips could stand a strain of more than 300% without breaking (330% for P10G15, 430% for P10G20, and 400% for P10G25), further demonstrating their good self-healing properties (Fig. 1c).

Finally, the self-healing performance was evaluated through rheology (Fig. 1d). At the strain of 0.1%, all the adhesive hydrogels showed gel-like behavior with the storage modulus G′ larger than the loss modulus G′′. When the strain was increased to 1200%, G′ decreased and was smaller than G′′, indicating a collapse of the adhesive network. However, when the strain was reverted from 1200% to 0.1%, G′′ again showed a larger value than G′. This process was repeated twice, clearly illustrating the self-healing properties of the adhesive hydrogels.

To study the self-healing properties at the micro level, the adhesive

hydrogels after self-healing were checked by optical microscopy and SEM. For the analysis by optical microscopy, two pieces with red and blue color were reconnected together after being broken. After incubation at 37 °C for 1 h, no obvious cracks were found under optical microscopy (Fig. 2a). Furthermore, the samples were also observed by the SEM after self-healing. There were still no obvious cracks at the interfaces as shown in Fig. 2a, when compared with the normal adhesive hydrogels (Fig. 2b). Hence, the optical microscopy and SEM further demonstrate the good self-healing properties of the hydrogels.

To further test if the self-healing leads to decreased mechanical properties, compression and tensile tests were carried out. Fig. 2c, d, and e showed that the compressive strength of the adhesive hydrogels before and after self-healing was almost the same at tested strain. The same phenomenon was observed for the tensile strength (Fig. 2f). These results show that the adhesive hydrogels can achieve both structural and mechanical self-healing.

The SEM analysis also showed that P10G15, P10G20, and P10G25 exhibited porous structures (Fig. 2b). The porous structure is advantageous in absorbing and retaining liquid in the moist environment while allowing nutrients exchange and metabolic waste transfer [19]. After the intrauterine application of the hydrogels, they will absorb body liquids consequently increasing their volume, which ensures that all the injured tissue can be effectively covered by the hydrogel [9]. As a result, hydrogel swelling is desirable in IUA prevention. Fig. S3a showed that all the formulations expressed swelling ability (252.1 ± 16.5% for P10G15, 251.9 ± 50.2% for P10G20, and 341.8 ± 30.5% for P10G25), making them promising in fully covering the damaged tissue. Degradability is another important property due to the need of a second surgery for removal of non-degradable materials. Thus, to verify the degradability of the hydrogels, the adhesive hydrogels were immersed into PBS at 37 °C and the weight change was recorded. Fig. S3b showed that all the formulations were degraded after 6–7 days. The biodegradability of these adhesive hydrogels resulted from the presence of the succinic ester in the structure [35].
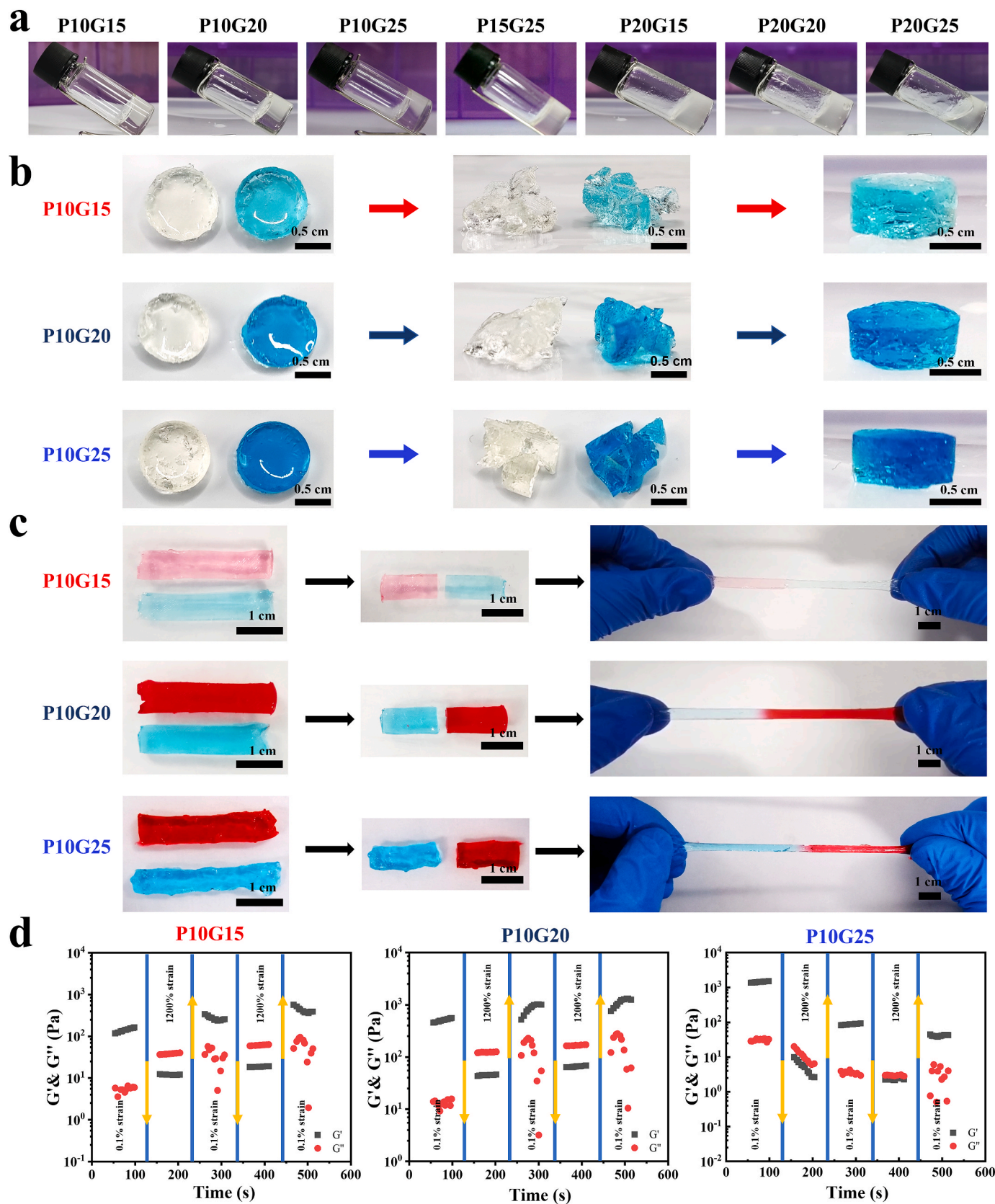
Fig. 1. The adhesive hydrogels showed self-healing properties. a) The hydrogels formed by mixing Bi-PEG-SS and gelatin at different concentrations with the same volume to get P10G15 (Bi-PEG-SS 10 wt%, Gelatin 15 wt%), P10G20 (Bi-PEG-SS 10 wt%, Gelatin 20 wt%), P10G25 (Bi-PEG-SS 10 wt%, Gelatin 25 wt%), P15G25 (Bi-PEG-SS 15 wt%, Gelatin 25 wt%), P20G15 (Bi-PEG-SS 20 wt%, Gelatin 15 wt%), P20G20 (Bi-PEG-SS 20 wt%, Gelatin 20 wt%), and P20G25 (Bi-PEG-SS 20 wt%, Gelatin 25 wt%). b) The performance of self-healing properties of P10G15, P10G20, and P10G25 when made into disc (Scale bar = 0.5 cm). c) The performance of self-healing properties of P10G15, P10G20, and P10G25 when made into strip (Scale bar = 1 cm). d,e,f) Dynamic strain cyclic tests (γ = 0.1% or 1200%) of P10G15 (d), P10G20 (e), and P10G25 (f) at 20 °C showing self-healing behavior.
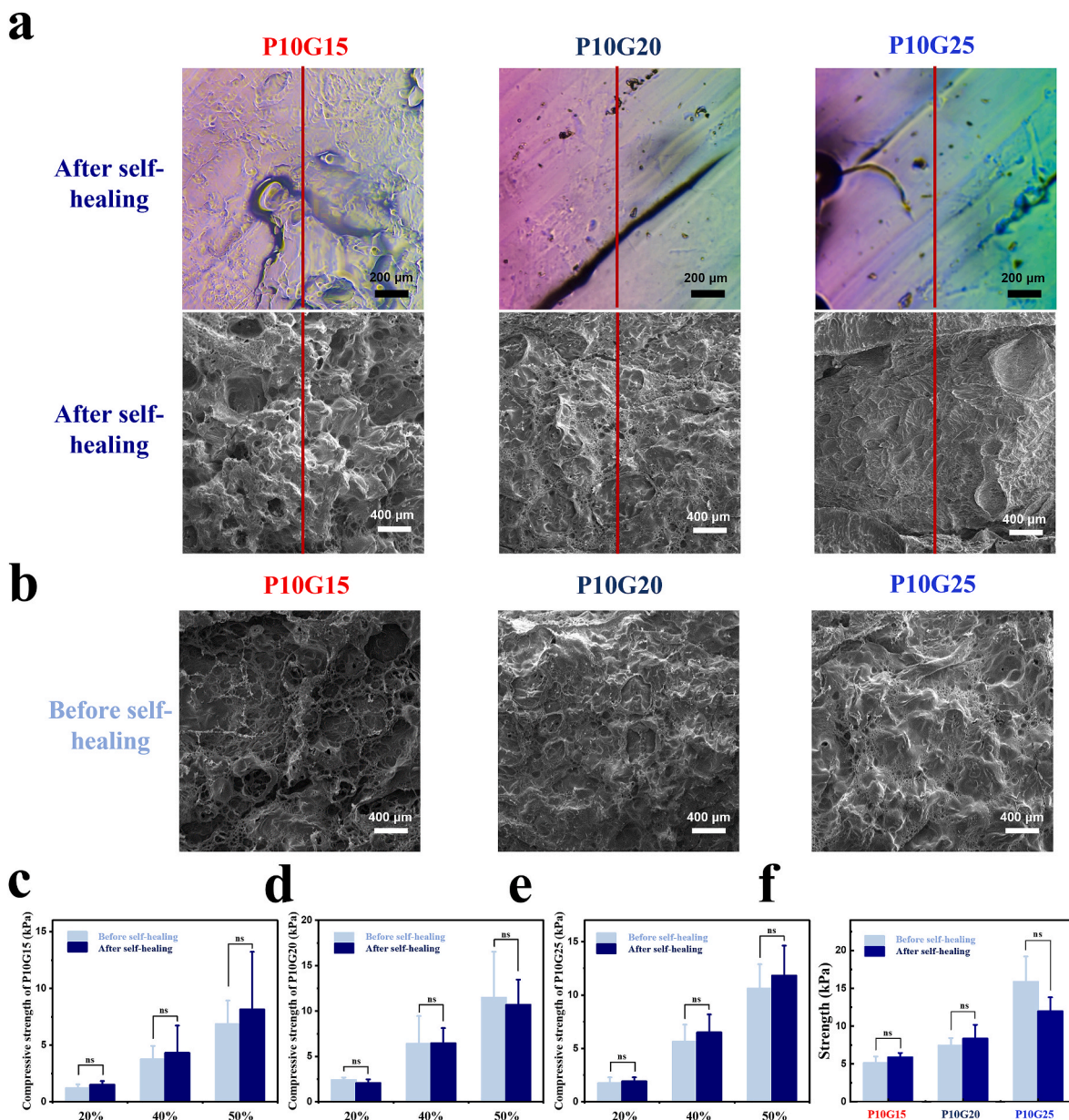
Fig. 2. Microstructure and mechanical properties of adhesive hydrogels before and after self-healing. a) Optical microscopy and SEM of adhesive hydrogels (P10G15, P10G20, and P10G25) after self-healing. (Red lines represent splicing areas, black scale bar = 200 μm, white scale bar = 400 μm) b) SEM of P10G15, P10G20, and P10G25 before self-healing. (White scale bar = 400 μm) c,d,e) The compressive strength of P10G15 (c), P10G20 (d), and P10G25 (e) after self-healing at strain of 20%, 40%, and 50% compared with those before self-healing. (n = 3, mean ± SD, ns: not significant) f) Tensile strength of P10G15, P10G20, and P10G25 before and after self-healing. (n = 3, mean ± SD, ns: not significant) Statistical significance was calculated with Student's t-test in b, c, d, and e.

3.2. Injectability, shape adaptability, and adhesion properties of the adhesive hydrogels

One of the main advantages of self-healing hydrogels is their inherent injectability [36]. It is pretty helpful in reducing the discomfort of both patients and clinicians when applying biomaterials [37]. As shown in Fig. 3a, all the adhesives could be easily injected into the different molds through a long and narrow catheter with an inner diameter of 1.5 mm. In real situations for IUA prevention, the hydrogels will be injected through the cervical canal, which offers limited space for the injection. Here, the ability to pass through the narrow catheter ensures that their application will not induce pain or discomfort to the patients. Once they were injected into the molds, they adapted to the mold structures, showing their potential to cover every corner of the uterus after injection (Fig. 3a). Meanwhile, after a second breakage, they

could again self-heal and adapt to the mold structure. These properties are critical for hydrogels intended to be injected through a narrow catheter. Even through their structure is broken during the injection, they will self-heal and adapt to the uterine cavity for the full cover once going into the uterus.

An in vivo injection in a female Sprague Dawley rat was further performed to demonstrate the injectability. Here, methylene blue-stained P10G20 was chosen as the representative formulation and injected through the rat's vagina. A catheter (Outer diameter of 1.5 mm; Inner diameter of 1 mm) was used for the injection. Fig. 3b and Video S1 (Video S1 was available in Supplementary data) showed that P10G20 was successfully injected into the rat's uterus through the vagina. After taking out the P10G20, it showed the shape of the rat's uterine cavity, with observed textures matching the uterine cavity. This experiment demonstrates that the adhesive hydrogels can be easily injected and
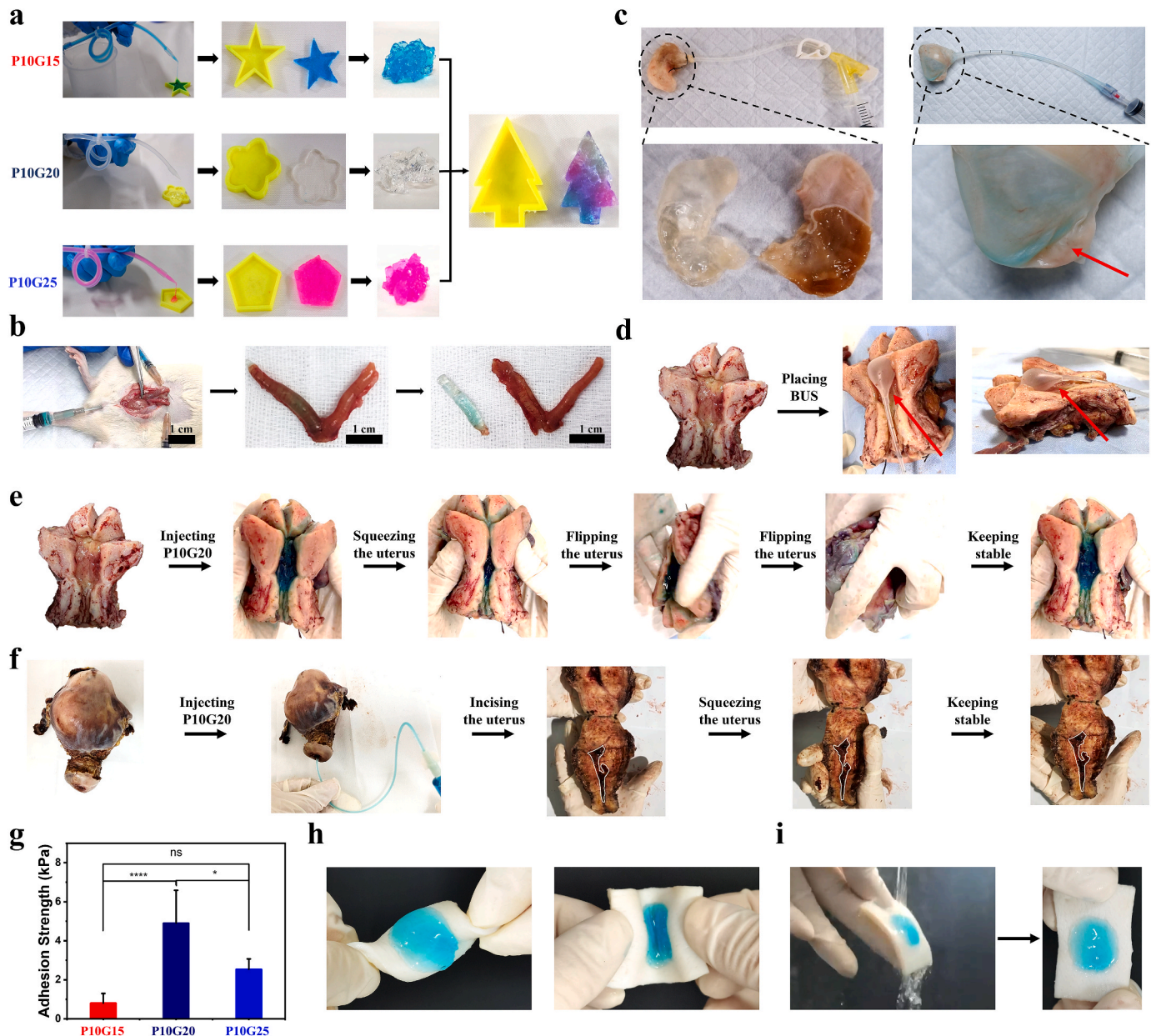
Fig. 3. The adhesive hydrogels showed self-adapting, self-healing and adhesion properties. a) The injectability, self-adapting and self-healing properties of P10G15, P10G20, and P10G25 in molds with different shapes. b) Photographs showing that the P10G20 was injected into the uterus through the vagina of the Sprague Dawley rat with a catheter of 1 mm diameter and adapted to the shape of the uterus. c) Photographs showing the self-adapting property of P10G20 in the stomach of the Sprague Dawley rat compared with BUS (The red arrow showed the unfilled cavity, Scale bar = 1 cm). d,e) Photographs showing the filling performance of BUS (d) and P10G20 (e) in the human uterus. The uterus was taken from a patient with ovarian cancer, which showed a uterine cavity similar to a healthy uterus. P10G20 kept stable in the uterus even under squeezing and flipping. (The red arrow shows the unfilled cavity). f) Photographs showing that P10G20 could be applied in irregular shape uterus with the disease. The uterus was taken from a patient with adenomyosis, which showed an extremely narrow uterine cavity. P10G20 kept stable under squeezing and flipping. g) Adhesion strength of P10G15, P10G20, and P10G25 (n = 5, mean ± SD, ns: not significant, *p < 0.05, ****p < 0.0001). h,i) Photographs showing the adhesion property of P10G20 on porcine skin under torsion (h) and water flow (i). Statistical significance was calculated with ANOVA with a Tukey post-hoc test in g.

adapt to the structure of the cavity.

Supplementary data related to this article can be found at https://doi.org/10.1016/j.bioactmat.2023.03.013.

Supplementary video related to this article can be found at https://doi.org/10.1016/j.bioactmat.2023.03.013

The problem with traditional BUS is that it can't cover every corner of the uterus, leaving a possibility for IUA in the uncovered areas [38]. Here, to show P10G20's advantage compared with traditional BUS, the rat stomach was used as a model (Fig. 3c). After the injection, P10G20 mechanically supported the stomach matrix without changing its shape.

When the adhesive was taken out, the surface of the adhesive presented the texture of the inner side of the stomach, further showing its adaptability to tissue. However, the use of BUS completely changed the shape of the stomach because of the mechanical pressure, following the actual situation when BUS was used. Besides, BUS didn't reach some areas of the stomach, showing that its use may leave uncovered places for tissue adhesion (Fig. 3c).

To further demonstrate the advantages of P10G20 over traditional BUS, the human uterus was used (Fig. 3d, e, and f). Firstly, a uterus from an ovarian cancer patient, which was fully opened, was collected. It

represented the normal uterus because its shape didn't change. Fig. 3d showed that traditional BUS still left some uncovered places in the uterus, as indicated by the red arrow. However, P10G20 entirely covered the uterus cavity (Fig. 3e), demonstrating its advantage in full coverage. In addition, BUS has shown significant limitations when preventing IUA in the uterus with pathological scenarios involving changed uterine shape. Here, a patient with adenomyosis was used as an example, whose uterine cavity becomes extremely narrow because of the disease (Fig. 3f). In this situation, BUS's application was challenging because of the narrowed cavity. On the contrary, P10G20 could still be injected into the cavity through a narrow catheter and fully cover the inside cavity (Fig. 3f). Altogether, the experiments with the human uterus show the advantages of P10G20 in fully covering both normal and abnormal uterine cavity compared to traditional BUS, illustrating its clinical potential in different scenarios.

Fig. 3e and f also showed that P10G20 kept stable in site after injection even with outside pressure or when the uteri were flipped, demonstrating its tissue adhesiveness. The adhesion resulted from the chemical bonds formed between Bi-PEG-SS and tissue protein through the ammonolysis reaction [35]. Good tissue adhesion can help maintain the stability of the adhesive hydrogel, thus contributing to the mechanical stability of the applied materials. Furthermore, the lap shear test was carried out to evaluate the adhesion strength. Fig. 3g showed

that all the formulations showed a certain value of adhesion strength (0.8 ± 0.5 kPa for P10G15, 4.9 ± 1.7 kPa for P10G20, and 2.5 ± 0.5 kPa for P10G25). For P10G20, the adhesion strength was the largest among all the groups tested. The adhesion performance of adhesive hydrogels was decided by the interfacial bonding strength and cohesion strength [39]. For the adhesive hydrogels, the interfacial bonding strength was achieved by the reaction between active ester from Bi-PEG-SS and amino groups from tissue protein. The cohesion strength formed because of the reaction between Bi-PEG-SS and gelatin. When the concentration of gelatin increased from 15 wt% to 20 wt%, the increased bulk intensity resulted in a more considerable cohesion strength because of more crosslinking, finally leading to a more significant adhesive strength. However, when the amount of gelatin was further increased to 25 wt%, more Bi-PEG-SS was consumed, leading to a weaker interface interaction and smaller adhesive strength. As a result, P10G20 possessed the highest adhesion strength among the tested groups. Fig. 3h and i showed that P10G20 kept stable on the porcine skin under torsion and water flow, further demonstrating its adhesiveness. Consequently, P10G20 was chosen for the rest of the experiments because of its best adhesion performance.
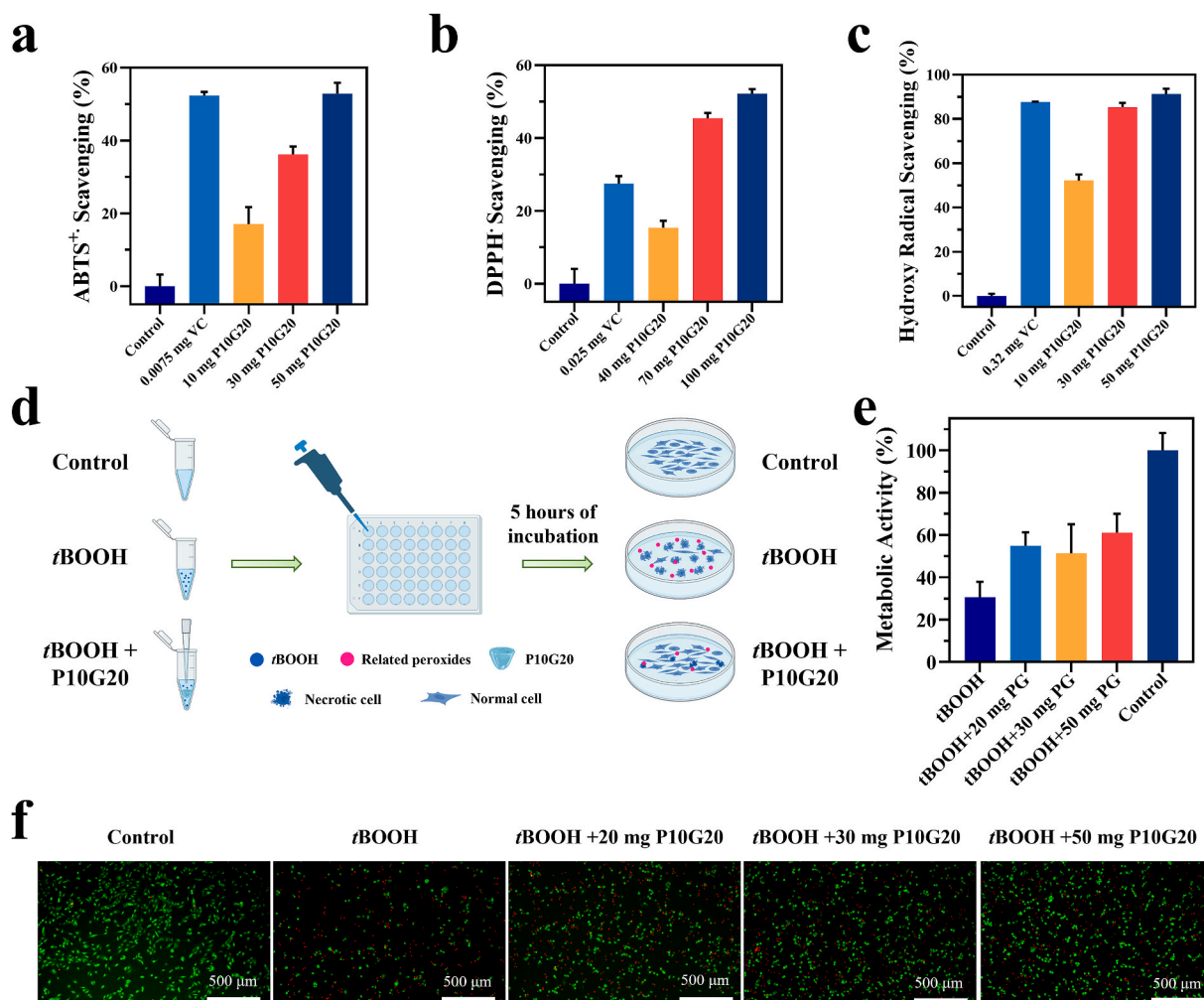

Fig. 4. P10G20 efficiently scavenges free radicals both in vitro and in cell culture. a,b,c) Results showing the scavenging rate of ABTS$^{+}\cdot$ (a), DPPH· (b), and hydroxy radical (c) by P10G20 compared with ascorbic acid solutions (VC). d) Scheme showing antioxidant cell model. The oxidative stress was induced by adding *tert*-butyl hydroperoxide solution (*t*BOOH). As control, the *t*BOOH and different weight of P10G20 were added together to show if P10G20 could rescue cells from oxidative stress caused by *t*BOOH. e,f) Metabolic activity (e) and live/dead cell staining (f) results of NIH3T3 cells when incubated with *t*BOOH alone and *t*BOOH with P10G20 of different weight. (Scale bar = 500 μm, n = 6, mean ± SD).

3.3. In vitro antioxidant properties of P10G20

Uterine injury, with the associated disruption of blood supply, results in local hypoxia, after which neutrophils and macrophages are recruited from the circulation and activated to do a burst release of free radicals [20,40]. Those free radicals further upregulate the production of TGF-β1 and VEGF, which are important regulators of fibrosis. They promote the secretion of extracellular matrix (ECM) and induce epithelial-mesenchymal cell transformation [41–43]. Besides, the over-expressed oxidative species cause lipid peroxidation, protein structure change, and DNA damage, subsequently impairing the healing of the uterus [23]. Gelatin, the hydrolysis product of collagen, was reported to have antioxidant properties [44–48]. Unlike synthetic antioxidants with potential hazards, gelatin is FDA-approved with well-defined biocompatibility. Here, we hypothesized that P10G20 would also show antioxidant properties since the engineered hydrogels were based on gelatin. To clarify this, P10G20's ability to scavenge different free radicals, including ABTS$^+$·, DPPH·, and hydroxyl radicals, was tested. Fig. 4a, b, and c showed that P10G20 scavenged different kinds of radicals with a dose-dependent behavior, indicating its good antioxidant properties. Thus, P10G20 can potentially reduce fibrosis by efficiently quenching the free radicals associated with oxidative stress.

The antioxidant properties are desirable for fibrosis inhibition but will also be helpful in reducing the tissue damage caused by oxidative stress to accelerate healing. To clarify it, a cell model of oxidative stress was established to prove if P10G20 can rescue cells [49]. As shown in Fig. 4d, tBOOH was chosen to induce oxidative stress in the cells, which resulted in cell apoptosis [50]. Thus, after adding tBOOH to the NIH 3T3 cells, the metabolic activity significantly decreased to 30.6 ± 5.9% (Fig. 4e). However, when adding P10G20 together to the cells, the metabolic activity nearly doubled and significantly increased to a value around 60%. The increased metabolic activity showed that P10G20 rescued the cells from oxidative stress. This was further clarified by using live/dead cell staining kit, showing that there were more live cells and fewer dead cells observed for P10G20-treated groups (Fig. 4f). Altogether, P10G20, with antioxidant properties, has the potential to inhibit tissue fibrosis and prevent tissue damage resulting from the oxidative stress.

3.4. In vitro biocompatibility of P10G20

According to the regulations of FDA and other different regions, safety is of equal importance as the efficacy of biomaterials [51]. Firstly, hemolytic and cell viability tests were carried out to test the safety of P10G20. The hemolytic test was performed since P10G20 will contact the wound and be exposed to the blood. The hemolysis ratio of the
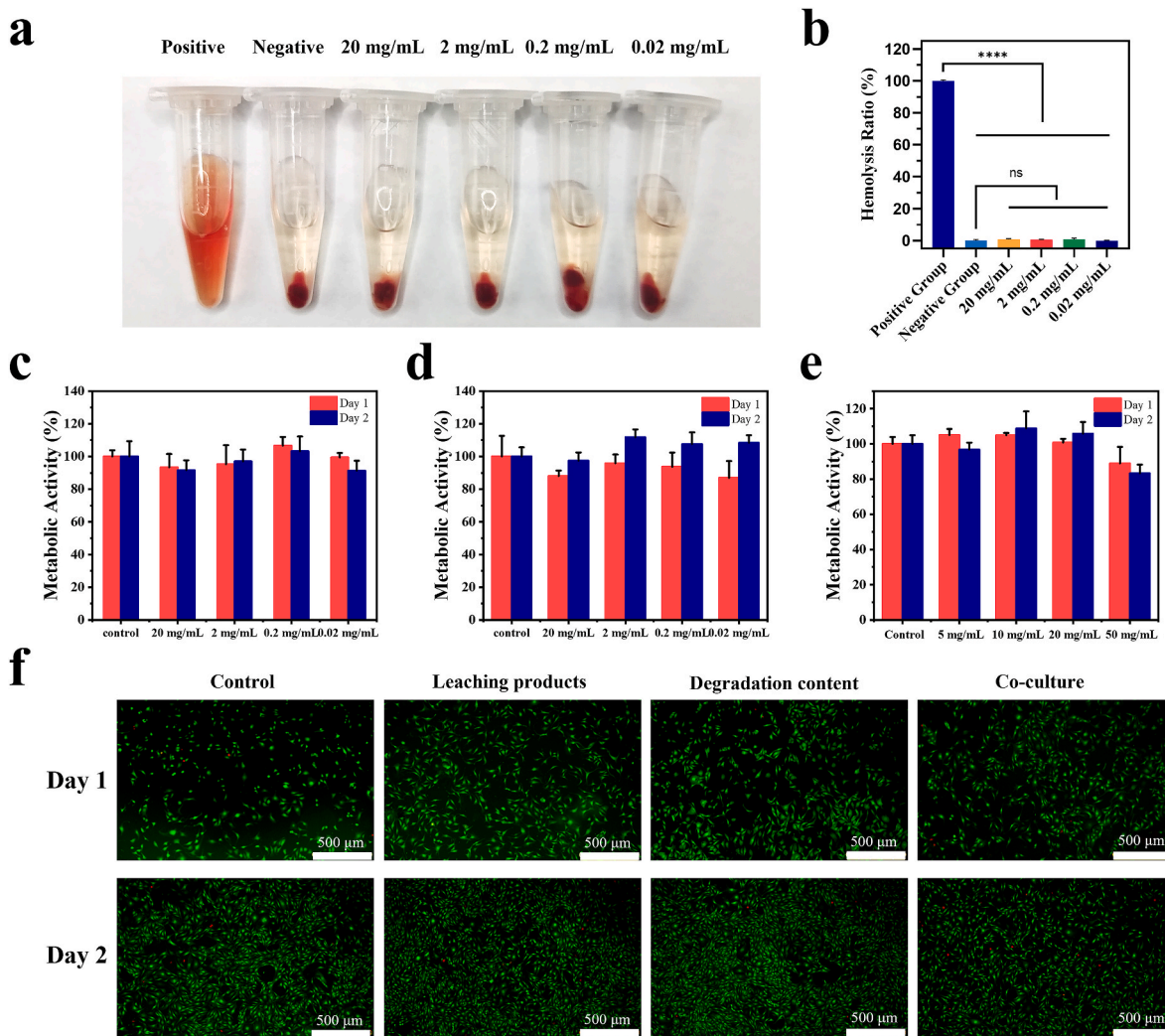
Fig. 5. P10G20 showed promising hemocompatibility and cytocompatibility in vitro. a,b) Picture (a) and result (b) showing the hemolysis rate of P10G20. (n = 3, mean ± SD, ns: not significant, ****p < 0.0001) c,d,e) Metabolic activity of NIH3T3 cells when incubated with leaching content of P10G20 (c) and degradation products of P10G20, (d) and co-cultured with P10G20 (e). f) Live/dead cell staining of NIH3T3 when incubated with leaching content of P10G20 and degradation products of P10G20, and co-cultured with P10G20. (Scale bar = 500 μm) Statistical significance was calculated with Dunnett post-hoc test in b.

P10G20 was very low at the tested concentrations, demonstrating good hemocompatibility (Fig. 5a and b). Furthermore, the metabolic activity tests showed that P10G20 did not affect cell viability, with values larger than 70% after being cultured with the leaching content (Fig. 5c), the degradation product (Fig. 5d), and P10G20 (Fig. 5e). The result was further confirmed by the live/dead cell staining, showing that there were few dead cells observed for the P10G20-treated cells (Fig. 5f). These in vitro experiments suggest that P10G20 may be a safe adhesive to be used in vivo.
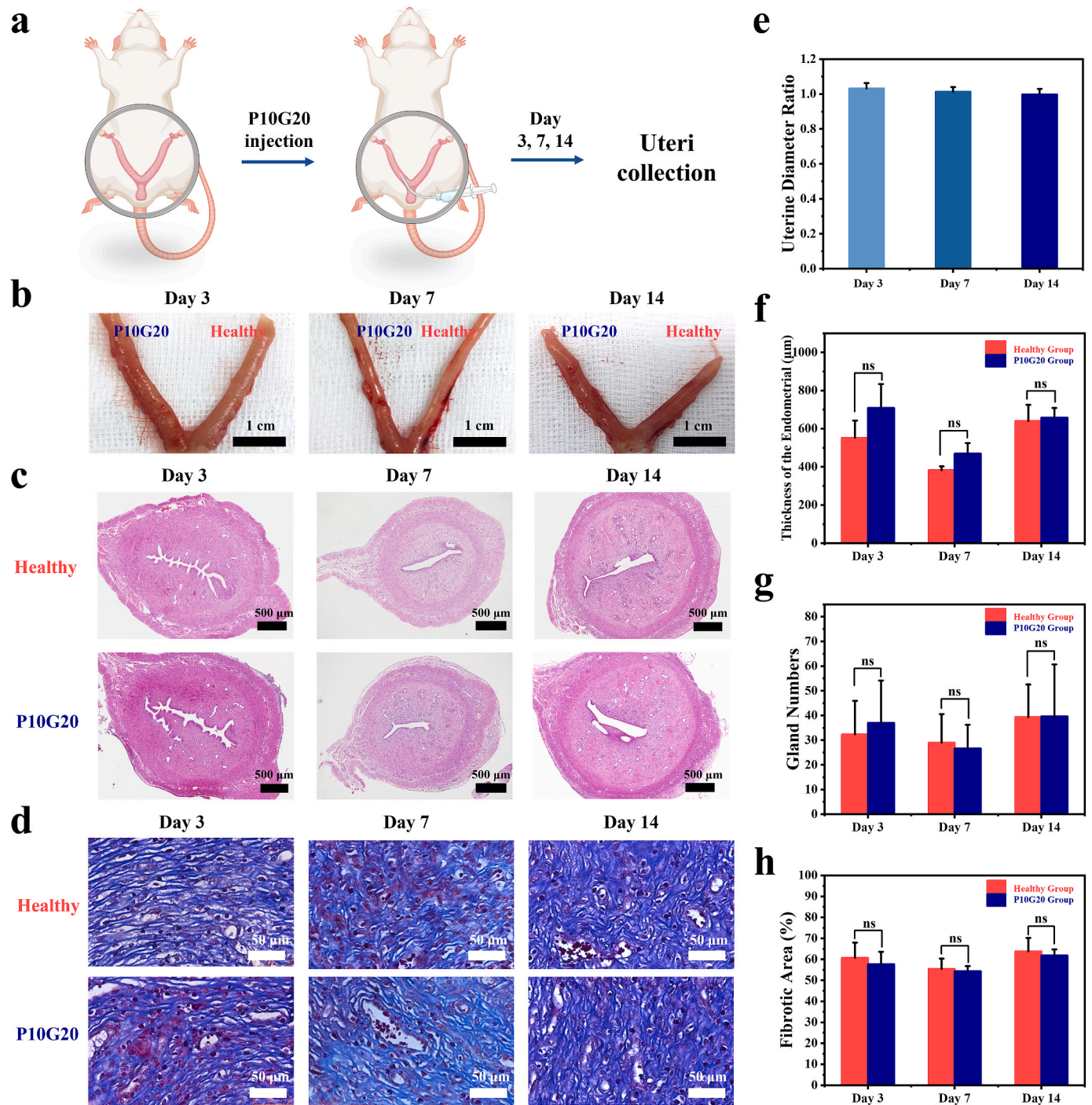

Fig. 6. P10G20 proved to be safe after being implanted in the Sprague Dawley rat uterus. a) Scheme showing that P10G20 was injected into one side of the rat uterus. At the chosen time points (Days 3, 4, and 14), the rats were sacrificed, and the uteri were observed. b) Pictures showing the results of rat uteri after hydrogel implantation on days 3, 7, and 14. (Scale bar = 1 cm) c,d) H&E (c) and Masson (d) staining results of the rat uteri on days 3, 7, and 14. (Black scale bar = 400 μm, white scale bar = 50 μm) e) The diameter ratio of the uterus side injected with P10G20 to the healthy side on days 3, 7, and 14. f) The results showing endometrial thickness of uteri after P10G20 implantation as calculated by H&E staining on days 3, 7, and 14. (n = 3, mean ± SD, ns: not significant) g) The results showing the number of endometrial glands of uteri after P10G20 implantation as calculated by H&E staining on days 3, 7, and 14. (n = 3, mean ± SD, ns: not significant) h) The results showing the area of endometrial fibrous tissue of uteri after P10G20 implantation as calculated by Masson staining on days 3, 7, and 14. (n = 3, mean ± SD, ns: not significant). Statistical significance was calculated with Student's t-test in f, g, and h.

3.5. In vivo biocompatibility of P10G20

To further show if P10G20 will cause any side effects when used in vivo, the implantation experiments were carried out by injecting P10G20 into one side of the Sprague Dawley rat's uterus (Fig. 6a). The other side of the uterus was used as the control (Healthy group). On days 3, 7, and 14 after the implantation, the rats were sacrificed, the uteri were visually checked, and H&E and Masson staining were carried out (Fig. 6b, c, and d). Fig. 5b showed that the sides of uteri with P10G20 didn't show any swelling and redness, indicating the excellent biocompatibility of the P10G20. The diameter ratio of the P10G20-implanted side to the healthy side was all close to 1 at the chosen time (1.03 ± 0.03 for day 3, 1.01 ± 0.02 for day 7, and 1.00 ± 0.03 for day 14), further confirming that P10G20 didn't induce any tissue swelling (Fig. 6e). Moreover, the H&E and Masson staining demonstrated that all the P10G20-treated uterus showed the similar staining results as those of the untreated sides (Fig. 6c and d). Besides, no significant differences were observed for the endometrial thickness and gland number, proving that P10G20 didn't induce any side effects in the uterus (Fig. 6f and g). Furthermore, the fibrosis area was calculated, demonstrating no increase in the fibrosis area after the implantation of P10G20 (Fig. 6h). The in vivo implantation assessments show that P10G20 possesses suitable features to be safely used in vivo.

3.6. In vivo IUA prevention with P10G20

Finally, the in vivo therapeutic efficacy of the adhesive hydrogels was evaluated using an IUA rat model. Briefly, the wounds were made on the rat's uterus using a homemade scraper. One side of the uterus was wounded. The other one was left untreated to act as the control to better compare the therapeutic efficacy (Fig. 7a). After scrabbing, it was easily observed that the thickness of the wounded uterus became thinner with bleeding (Fig. 7b). Afterwards, the hydrogels were injected. As bioadhesives showed the ability to seal leakage, we hypothesized that the P10G20 might also be beneficial in preventing blood leakage [52], which was also the reason for post-operative adhesion [52,53]. 7 days later, the rats were sacrificed, and H&E and Masson staining were carried out (Fig. 7b, c, and d). Fig. 7b showed that for the Saline group, the injured half is swelling, with a significantly larger diameter than the healthy ones with a ratio of 1.29 ± 0.12 (Fig. 7e). On the control, the diameter of P10G20 group was nearly the same as that of the health side with a ratio of 1.07 ± 0.04 (Fig. 7b and e). We deduced this happened because of increased fibrosis in the control group. Once the uterus was harvested, it got smaller because of tissue shrinkage. However, for the Saline group, the fibrotic tissue stopped the tissue shrinkage, leading to a larger diameter postmortem. Besides, there was more obstruction observed when trying to inject methylene blue solution through the Saline group compared to that of P10G20 group, showing that there was more tissue adhesion in the Saline group (Videos S2 and S3 were available in Supplementary data). Furthermore, the thickness of the endometrium and the number of glands were calculated (Fig. 7f and g). For the thickness of the endometrium, P10G20 group (463.6 ± 62.7 μm) showed a similar value to that of the healthy group (489.0 ± 97.1 μm), with a more considerable value compared with the Saline group (402.4 ± 79.0 μm). Regarding the number of glands, the same trend was observed. The Saline group showed the smallest average number of glands (8.7 ± 6.3), while the number of P10G20 group (13.0 ± 5.1) was similar to that of healthy groups (14.6 ± 5.6), without statistically significant differences. Furthermore, the fibrosis area was calculated using Masson staining (Fig. 7h). Saline-treated group showed a significantly larger value of fibrosis area when compared with the healthy group. In contrast, P10G20-treated group showed a similar state as the healthy group. In summary, animal studies show that P10G20 effectively inhibits the fibrosis of the uterus and maintains a uterus condition identical to the healthy tissue.

Supplementary data related to this article can be found at https://doi .org/10.1016/j.bioactmat.2023.03.013.

Supplementary video related to this article can be found at https:// doi.org/10.1016/j.bioactmat.2023.03.013

## 3.7. Determination of H_2O_2 content and expression levels of related fibrosis factors in rats

High levels of oxidative stress promoted adhesion formation [20]. Our in vitro experiments demonstrated that P10G20 had antioxidant properties which quenched free radicals and rescued cells from oxidative damage. To verify the in vivo antioxidant performance, FOX1 experiments were performed with tissue homogenates, and H_2O_2 was used to indicate the oxidative stress in the tissue [54]. As shown in Fig. 8, compared with the saline-treated group, P10G20-treated group demonstrated significantly lower H_2O_2 amount after 12 h of surgery (Fig. 8a). The similar trend was observed at day 1, which showed that P10G20 decreased the in vivo oxidative stress (Fig. 8b). At day 3 and day 7, all the groups showed H_2O_2 level without significant difference, which may result from the degradation of P10G20 and the healing of the tissue (Fig. 8c and d). However, P10G20-treated group and the healthy group still expressed lower average value than that of the saline-treated group. The in vivo oxidative stress experiments demonstrate that P10G20 can decrease the oxidative stress at the beginning of wound healing which may help slow the progression of fibrosis.

Later, the qRT-PCR was carried out to detect the fibrosis-related cytokines. TGF-β1 disrupts the degradation of ECM and leads to the uncontrolled fibrotic response by inhibiting the expression and activity of matrix metalloproteinases [10,20,55,56]. The qRT-PCR results showed that at the chosen time, P10G20-treated uteri showed significantly lower expression of TGF-β1 compared to that of the Saline-treated group (Fig. 8e and f). These findings indicate that P10G20 downregulates the expression of TGF-β1, which may result from the generation of a more amenable environment due to the antioxidant properties of P10G20.

VEGF is another major cytokine involved in tissue fibrosis and IUA [43], which promotes angiogenesis and induces fibrosis of endometrium by culminating in cellular migration, mitosis, and proliferation [57]. The oxidative stress related to IUA also leads to the increase of VEGF expression and results in enhanced ECM deposition and adhesion development. Fig. 8g and h showed that P10G20 significantly decreased the expression of VEGF compared to the Saline group, illustrating declined severity of tissue adhesion. Altogether, the qRT-PCR experiments demonstrate that P10G20 effectively prevents IUA through downregulating TGF-β1 and VEGF, thus inhibiting ECM deposition and promoting ECM degradation (Fig. 8i).

4. Conclusion

In this study, we report an adhesive hydrogel fabricated by Bi-PEG-SS and gelatin for IUA prevention. The adhesive hydrogel exhibited self-healing properties with good injectability, providing convenience in the application and being able to cover every corner of the uterus. It also possessed good cytocompatibility, hemocompatibility and in vivo biocompatibility. The in vivo studies showed that the adhesive hydrogel effectively stopped the IUA with less area of endometrial fibrous tissue. Considering that Bi-PEG-SS and gelatin have a good FDA history, these adhesive hydrogels might offer a new alternative to the IUA therapy. However, authors believe that there are still some concerns and questions to be addressed before the hydrogels can really reach clinics. First, the degradation range of these hydrogels should be further expanded to solve the contradiction between efficacy and different species. In addition, all experiments presented here were carried out using rodent models. Authors consider that the study of the adhesive hydrogels in large animal models is needed to further demonstrate the performance of those hydrogels in different species.
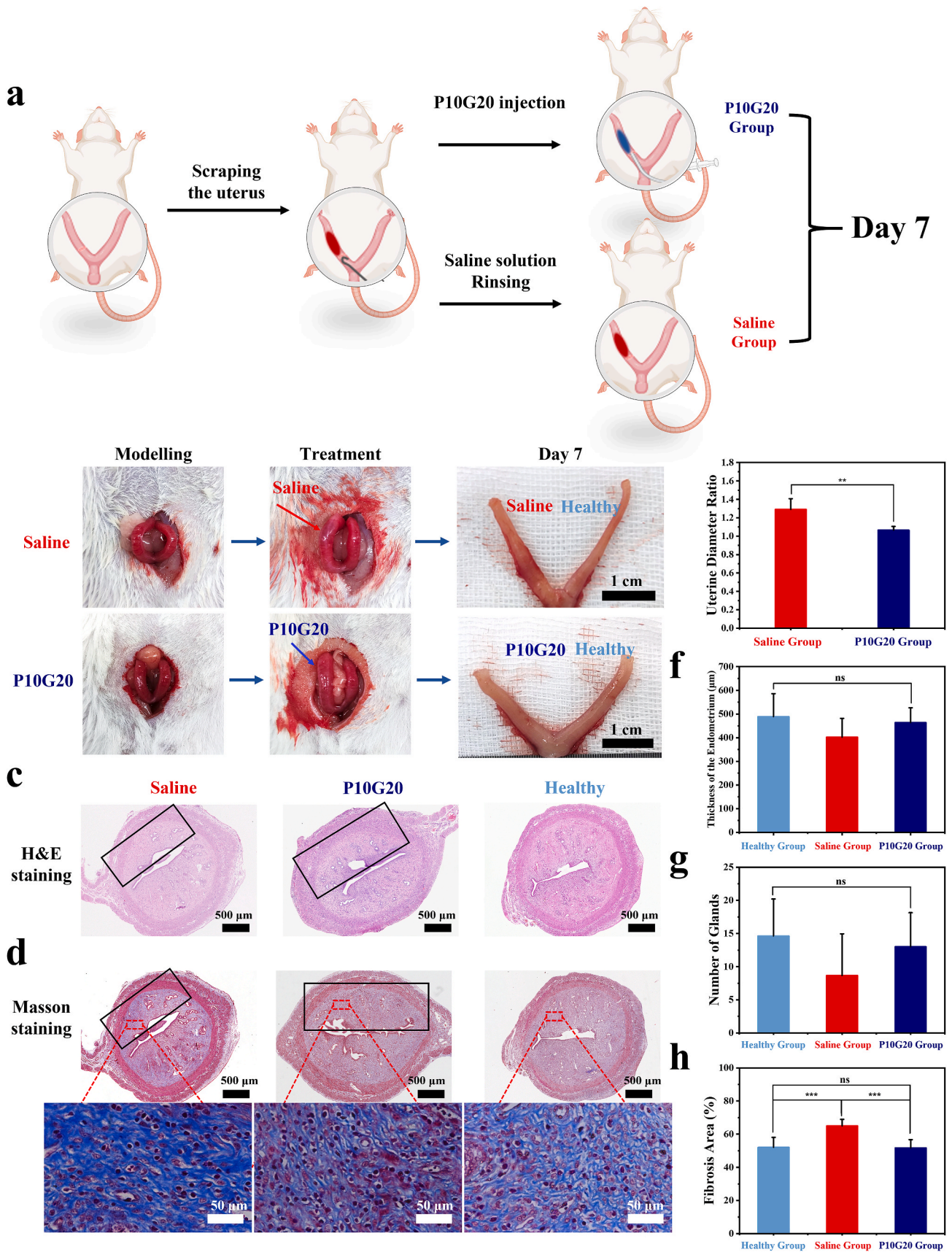
(caption on next page)

Fig. 7. P10G20 showed promising therapeutic potential in an in vivo model of IUA. a) Scheme showing that the endometrium was scratched with a curved hook to build the IUA model. P10G20 group received an injection of P10G20. The Saline group was rinsed with saline solution. The healthy uterus was used as the control. b) Pictures showing the process of the experiments, including modelling, saline, and P10G20 treatment, and tissue observation on day 7. Scale bar = 1 cm. c,d) H&E (c) and Masson (d) staining results of the rat uteri in different groups on day 7. The parts inside the black frame are the wounded uterine areas. (Black scale bar = 600 μm, white scale bar = 50 μm. e) The ratio of uterine diameter in the P10G20 and Saline groups to those of the healthy group on day 7. (n = 6, mean ± SD, **p < 0.01) f) The results showing endometrial thickness in different groups calculated by H&E staining on day 7. (n = 6, mean ± SD, ns: not significant) g) The results showing the number of endometrial glands in different groups calculated by H&E staining on day 7. (n = 6, mean ± SD, ns: not significant) h) The results showing the endometrial fibrous tissue area in different groups calculated by Masson staining on day 7. (n = 6, mean ± SD, ns: not significant, ***p < 0.001) Statistical significance was calculated with Student's t-test in e, f, and g, with ANOVA with a Tukey post-hoc test in h.
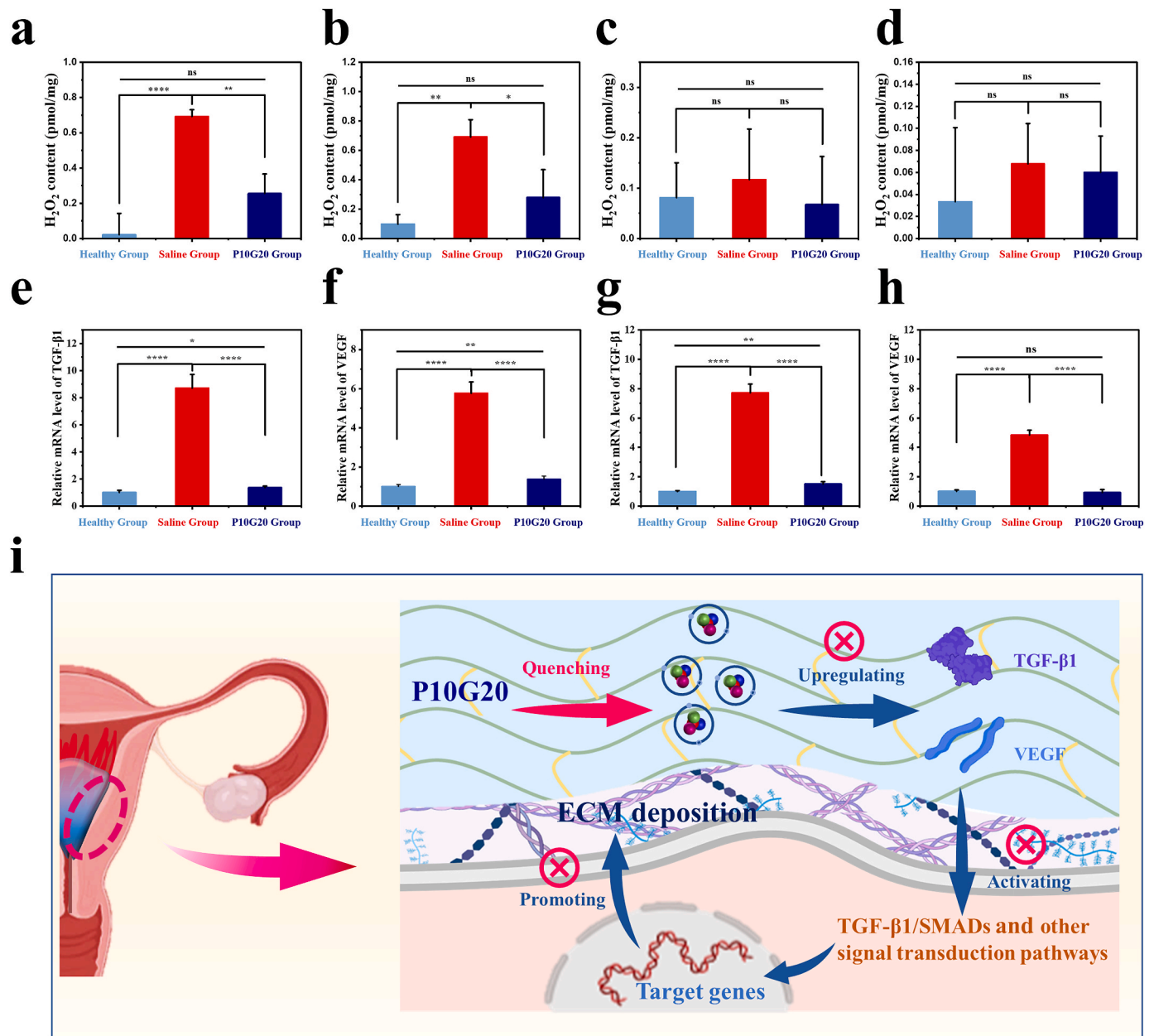

Fig. 8. In vivo P10G20 antioxidation and antifibrosis tests. a,b,c,d) The content of H_2O_2 in uterine tissue on day 0.5 (a), day 1 (b), day 3 (c), and day 7 (d) post-surgery. (n = 3, mean ± SD, ns: not significant, *p < 0.05, **p < 0.01, ****p < 0.0001) e,f) Relative mRNA level of TGF-β1 in rat uteri on day 1 (e) and day 3 (f). (n = 3, mean ± SD, *p < 0.05, **p < 0.01, ****p < 0.0001) g,h) Relative mRNA level of VEGF in rat uteri on day 1 (g) and day 3 (h). (n = 3, mean ± SD, ns: not significant, **p < 0.01, ****p < 0.0001) i) Scheme showing that the antioxidant properties of P10G20 slowed down the occurrence of oxidative stress in tissue, which downregulated the levels of TGF-β1 and VEGF. The decreased fibrosis-related cytokines reduced the deposition of the ECM, which inhibited IUA development. Statistical significance was calculated with ANOVA with a Tukey post-hoc test in a, b, c, d, e, f, g, and h.

Ethics approval and consent to participate

All animal experiments were performed in accordance with the 'Principles of Laboratory Animal Care'(NIH) and guidelines of the laboratory animal care committee of Xi'an Jiaotong University (No: 2021-213).

The human uteri were used under the approval of Medical Ethics Committee of Jiangxi Maternal and Child Health Hospital (No: EC-KT-202143). The use had also been approved by the patients.

CRediT authorship contribution statement

Luyao Feng: Investigation, Methodology, Data curation, Formal analysis, Software, Validation, Writing – original draft. **Liqun Wang:** Conceptualization, Methodology, Formal analysis, Funding acquisition, Writing – review & editing. **Yao Ma:** Investigation, Data curation. **Wanglin Duan:** Investigation, Formal analysis. **Sergio Martin-Saldaña:** Visualization, Writing – review & editing. **Ye Zhu:** Investigation, Writing – review & editing. **Xianpeng Zhang:** Software. **Bin Zhu:** Investigation, Writing – review & editing. **Chaowei Li:** Writing – review & editing. **Shibo Hu:** Investigation. **Mingjie Bao:** Data curation. **Ting Wang:** Data curation. **Yuan Zhu:** Investigation, Data curation, Funding acquisition, Project administration. **Fei Yang:** Conceptualization, Resources, Project administration. **Yazhong Bu:** Conceptualization, Writing – review & editing, Resources, Supervision, Funding acquisition, Project administration.

Declaration of competing interest

All authors declared no competing interests.

Acknowledgments

Appendix A. Supplementary data

Supplementary data to this article can be found online at https://doi.org/10.1016/j.bioactmat.2023.03.013.

References

[1] S. Zhang, W. Xia, J. Xu, H. Xu, C. Lu, Y. Zhao, X. Wu, Three-dimensional structure micelles of heparin-poloxamer improve the therapeutic effect of 17β-estradiol on endometrial regeneration for intrauterine adhesions in a rat model, Int. J. Nanomed. 12 (2017) 5643–5657, https://doi.org/10.2147/ijn.S137237.

[2] J. Wang, C. Yang, Y. Xie, X. Chen, T. Jiang, J. Tian, S. Hu, Y. Lu, Application of bioactive hydrogels for functional treatment of intrauterine adhesion, Front. Bioeng. Biotechnol. 9 (2021), 760943, https://doi.org/10.3389/fbioe.2021.760943.

[3] C. Wei, Y. Pan, Y. Zhang, Y. Dai, L. Jiang, L. Shi, W. Yang, S. Xu, Y. Zhang, W. Xu, Y. Zhang, X. Lin, S. Zhang, Correction: overactivated sonic hedgehog signaling aggravates intrauterine adhesion via inhibiting autophagy in endometrial stromal cells, Cell Death Dis. 11 (2020) 935, https://doi.org/10.1038/s41419-020-03128-y.

[4] M.M. Hanstede, E. van der Meij, L. Goedemans, M.H. Emanuel, Results of centralized Asherman surgery, Fertil. Steril. 104 (2015) 1561–1568, https://doi.org/10.1016/j.fertnstert.2015.08.039, 2003-2013.

[5] R.F. Valle, J.J. Sciarra, Intrauterine adhesions: hysteroscopic diagnosis, classification, treatment, and reproductive outcome, Am. J. Obstet. Gynecol. 158 (1988) 1459–1470.

[6] H. Fernandez, F. Al-Najjar, A. Chauveaud-Lambling, R. Frydman, A. Gervaise, Fertility after treatment of Asherman's syndrome stage 3 and 4, J. Minim. Invasive Gynecol. 13 (2006) 398–402, https://doi.org/10.1016/j.jmig.2006.04.013.

[7] H. Xu, J. Xu, B. Shen, S. Zhang, B. Jin, Q. Zhu, D. ZhuGe, X. Wu, J. Xiao, Y. Zhao, Dual regulations of thermosensitive heparin–poloxamer hydrogel using ε-Polylysine: bioadhesivity and controlled KGF release for enhancing wound healing of endometrial injury, ACS Appl. Mater. Interfaces 9 (2017) 29580–29594, https://doi.org/10.1021/acsami.7b10211.

[8] X. Zhang, G. Chen, Y. Wang, L. Fan, Y. Zhao, Arrowhead composite microneedle patches with anisotropic surface adhesion for preventing intrauterine adhesions, Adv. Sci. 9 (2022), e2104883, https://doi.org/10.1002/advs.202104883.

[9] Y. Cai, F. Wu, Y. Yu, Y. Liu, C. Shao, H. Gu, M. Li, Y. Zhao, Porous scaffolds from droplet microfluidics for prevention of intrauterine adhesion, Acta Biomater. 84 (2019) 222–230, https://doi.org/10.1016/j.actbio.2018.11.016.

[10] L. Kou, X. Jiang, S. Xiao, Y. Zhao, Q. Yao, R. Chen, Therapeutic options and drug delivery strategies for the prevention of intrauterine adhesions, J. Contr. Release 318 (2020) 25–37, https://doi.org/10.1016/j.jconrel.2019.12.007.

[11] B. Wang, C. Feng, J. Dang, Y. Zhu, X. Yang, T. Zhang, R. Zhang, J. Li, J. Tang, C. Shen, L. Shen, J. Dong, X. Zhang, Preparation of fibroblast suppressive poly (ethylene glycol)-b-poly(l-phenylalanine)/Poly(ethylene glycol) hydrogel and its application in intrauterine fibrosis prevention, ACS Biomater. Sci. Eng. 7 (2021) 311–321, https://doi.org/10.1021/acsbiomaterials.0c01390.

[12] S. Xiao, Y. Wan, M. Xue, X. Zeng, F. Xiao, D. Xu, X. Yang, P. Zhang, W. Sheng, J. Xu, S. Zhou, Etiology, treatment, and reproductive prognosis of women with moderate-to-severe intrauterine adhesions, Int. J. Gynecol. Obstet. 125 (2014) 121–124, https://doi.org/10.1016/j.ijgo.2013.10.026.

[13] Y. Chi, P. He, L. Lei, Y. Lan, J. Hu, Y. Meng, L. Hu, Transdermal estrogen gel and oral aspirin combination therapy improves fertility prognosis via the promotion of endometrial receptivity in moderate to severe intrauterine adhesion, Mol. Med. Rep. 17 (2018) 6337–6344, https://doi.org/10.3892/mmr.2018.8685.

[14] E.M. Ahmed, Hydrogel: preparation, characterization, and applications: a review, J. Adv. Res. 6 (2015) 105–121, https://doi.org/10.1016/j.jare.2013.07.006.

[15] A.S. Hoffman, Hydrogels for biomedical applications, Adv. Drug Deliv. Rev. 64 (2012) 18–23, https://doi.org/10.1016/j.addr.2012.09.010.

[16] F. Liu, S. Hu, H. Yang, Z. Li, K. Huang, T. Su, S. Wang, K. Cheng, Hyaluronic acid hydrogel Integrated with mesenchymal stem cell-secretome to treat endometrial injury in a rat model of asherman's syndrome, Adv. Healthcare Mater. 8 (2019), e1900411, https://doi.org/10.1002/adhm.201900411.

[17] H. An, L. Zhu, J. Shen, W. Li, Y. Wang, J. Qin, Self-healing PEG-poly(aspartic acid) hydrogel with rapid shape recovery and drug release, Colloids Surf., B 185 (2020), 110601, https://doi.org/10.1016/j.colsurfb.2019.110601.

[18] L. Zhou, C. Dai, L. Fan, Y. Jiang, C. Liu, Z. Zhou, P. Guan, Y. Tian, J. Xing, X. Li, Y. Luo, P. Yu, C. Ning, G. Tan, Injectable self-healing natural biopolymer-based hydrogel adhesive with thermoresponsive reversible adhesion for minimally invasive surgery, Adv. Funct. Mater. 31 (2021), 2007457, https://doi.org/10.1002/adfm.202007457.

[19] H. Lv, B. Wu, J. Song, W. Wu, W. Cai, J. Xu, Hydrogel, a novel therapeutic and delivery strategy, in the treatment of intrauterine adhesions, J. Mater. Chem. B 9 (2021) 6536–6552, https://doi.org/10.1039/d1tb01005k.

[20] A.O. Awonuga, J. Belotte, S. Abuanzeh, N.M. Fletcher, M.P. Diamond, G.M. Saed, Advances in the pathogenesis of adhesion development: the role of oxidative stress, Reprod. Sci. 21 (2014) 823–836, https://doi.org/10.1177/1933719114522550.

[21] B. Li, Q. Zhang, J. Sun, D. Lai, Human amniotic epithelial cells improve fertility in an intrauterine adhesion mouse model, Stem Cell Res. Ther. 10 (2019) 257, https://doi.org/10.1186/s13287-019-1368-9.

[22] W. Zhang, Y. Yuan, G. Huang, J. Xiao, Potential molecular mechanism of guishen huoxue decoction against intrauterine adhesion based on network pharmacology, Evid.-Based Complement. Altern. Med. (2022), 4049147, https://doi.org/10.1155/2022/4049147, 2022.

[23] J. Lu, Z. Wang, J. Cao, Y. Chen, Y. Dong, A novel and compact review on the role of oxidative stress in female reproduction, Reprod. Biol. Endocrinol. 16 (2018) 80, https://doi.org/10.1186/s12958-018-0391-5.

[24] S. Shabanian, M. Khazaie, G.A. Ferns, M. Arjmand, Local renin-angiotensin system molecular mechanisms in intrauterine adhesions formation following gynecological operations, new strategy for novel treatment, J. Obstet. Gynaecol. 42 (2022) 1613–1618, https://doi.org/10.1080/01443615.2022.2036972.

[25] H. Li, Y. Tan, S. Liu, L. Li, Three-dimensional bioprinting of oppositely charged hydrogels with super strong interface bonding, ACS Appl. Mater. Interfaces 10 (2018) 11164–11174, https://doi.org/10.1021/acsami.7b19730.

[26] C. He, X. Xu, Y. Lin, Y. Cui, Z. Peng, A bilayer skin-inspired hydrogel with strong bonding interface, Nanomaterials 12 (2022) 1137, https://doi.org/10.3390/nano12071137.

[27] W. Duan, L. Zhang, R. Bohara, S. Martin-Saldana, F. Yang, Y. Zhao, Y. Xie, Y. Bu, A. Pandit, Adhesive hydrogels in osteoarthritis: from design to application, Mil. Med. Res. 10 (2023) 4, https://doi.org/10.1186/s40779-022-00439-3.

[28] L.M. Ensign, B.C. Tang, Y. Wang, T.A. Tse, T. Hoen, R. Cone, J. Hanes, Mucus-penetrating nanoparticles for vaginal drug delivery protect against herpes simplex virus, Sci. Transl. Med. 4 (2012), https://doi.org/10.1126/scitranslmed.3003453, 138ra179.

[29] P. Wang, Y. Zhu, L. Feng, Y. Wang, Y. Bu, Rapidly self-deactivating and injectable succinyl ester-based bioadhesives for postoperative antiadhesion, ACS Appl. Mater. Interfaces 14 (2022) 373–382, https://doi.org/10.1021/acsami.1c21083.

[30] K. Ren, Y. Cheng, C. Huang, R. Chen, Z. Wang, J. Wei, Self-healing conductive hydrogels based on alginate, gelatin and polypyrrole serve as a repairable circuit and a mechanical sensor, J. Mater. Chem. B 7 (2019) 5704–5712, https://doi.org/10.1039/c9tb01214a.

[31] G. Lyngsie, L. Krumina, A. Tunlid, P. Persson, Generation of hydroxyl radicals from reactions between a dimethoxyhydroquinone and iron oxide nanoparticles, Sci. Rep. 8 (2018), 10834, https://doi.org/10.1038/s41598-018-29075-5.

[32] O. Erel, A new automated colorimetric method for measuring total oxidant status, Clin. Biochem. 38 (2005) 1103–1111, https://doi.org/10.1016/j.clinbiochem.2005.08.008.

[33] A. Duconseille, T. Astruc, N. Quintana, F. Meersman, V. Sante-Lhoutellier, Gelatin structure and composition linked to hard capsule dissolution: a review, Food Hydrocolloids 43 (2015) 360–376, https://doi.org/10.1016/j.foodhyd.2014.06.006.

[34] T.M.T. Sakai, Y. Yamamoto, C. Ito, R. Yoshida, S. Suzuki, N. Sasaki, M. Shibayam, U.-i. Chung, Design and fabrication of a high-strength hydrogel with ideally homogeneous network structure from tetrahedron-like macromonomers, Macromolecules 41 (2008) 5379–5384, https://doi.org/10.1021/ma800476x.

[35] Y. Bu, L. Zhang, G. Sun, F. Sun, J. Liu, F. Yang, P. Tang, D. Wu, Tetra-PEG based hydrogel sealants for in vivo visceral hemostasis, Adv. Mater. 31 (2019), 1901580, https://doi.org/10.1002/adma.201901580.

[36] S. Li, L. Wang, W. Zheng, G. Yang, X. Jiang, Rapid fabrication of self-healing, conductive, and injectable gel as dressings for healing wounds in stretchable parts of the body, Adv. Funct. Mater. 30 (2020), 2002370, https://doi.org/10.1002/adfm.202002370.

[37] V.K.A. Devi, R. Shyam, A. Palaniappan, A.K. Jaiswal, T.H. Oh, A.J. Nathanael, Self-healing hydrogels: preparation, mechanism and advancement in biomedical applications, Polymers 13 (2021) 3782, https://doi.org/10.3390/polym13213782.

[38] J. Bosteels, S. Weyers, T.M. D'Hooghe, H. Torrance, F.J. Broekmans, S.J. Chua, B. W.J. Mol, Anti-adhesion therapy following operative hysteroscopy for treatment of female subfertility, Cochrane Database Syst. Rev. 11 (2017), CD011110, https://doi.org/10.1002/14651858.CD011110.pub3.

[39] Y. Bu, A. Pandit, Cohesion mechanisms for bioadhesives, Bioact. Mater. 13 (2022) 105–118, https://doi.org/10.1016/j.bioactmat.2021.11.008.

[40] C. Murdoch, C.E. Lewis, Macrophage migration and gene expression in response to tumor hypoxia, Int. J. Cancer 117 (2005) 701–708, https://doi.org/10.1002/ijc.21422.

[41] X. Meng, D.J. Nikolic-Paterson, H. Lan, TGF-beta: the master regulator of fibrosis, Nat. Rev. Nephrol. 12 (2016) 325–338, https://doi.org/10.1038/nrneph.2016.48.

[42] S. Liu, X. Huang, Y. Liu, D. Song, Y. Xiao, Functional analysis of miRNAs combined with TGF-β1/Smad3 inhibitor in an intrauterine rat adhesion cell model, Mol. Cell. Biochem. 470 (2020) 15–28, https://doi.org/10.1007/s11010-020-03741-7.

[43] J. Zhang, M. Chu, Differential roles of VEGF: relevance to tissue fibrosis, J. Cell. Biochem. 120 (2019) 10945–10951, https://doi.org/10.1002/jcb.28489.

[44] P. Phanturat, S. Benjakul, W. Visessanguan, S. Roytrakul, Use of pyloric caeca extract from bigeye snapper (Priacanthus macracanthus) for the production of gelatin hydrolysate with antioxidative activity, LWT–Food Sci. Technol. 43 (2010) 86–97, https://doi.org/10.1016/j.lwt.2009.06.010.

[45] P.A. Harnedy, R.J. FitzGerald, Bioactive peptides from marine processing waste and shellfish: a review, J. Funct.Foods 4 (2012) 6–24, https://doi.org/10.1016/j.jff.2011.09.001.

[46] T. Senphan, S. Benjakul, Antioxidative activities of hydrolysates from seabass skin prepared using protease from hepatopancreas of Pacific white shrimp, J. Funct. Foods 6 (2014) 147–156, https://doi.org/10.1016/j.jff.2013.10.001.

[47] B. Li, F. Chen, X. Wang, B. Ji, Y. Wu, Isolation and identification of antioxidative peptides from porcine collagen hydrolysate by consecutive chromatography and electrospray ionization–mass spectrometry, Food Chem. 102 (2007) 1135–1143, https://doi.org/10.1016/j.foodchem.2006.07.002.

[48] T. Senphan, S. Benjakul, Use of the combined phase partitioning systems for recovery of proteases from hepatopancreas of Pacific white shrimp, Sep. Purif. Technol. 129 (2014) 57–63, https://doi.org/10.1016/j.seppur.2014.03.025.

[49] Y. Bu, W. Zhang, S. Martin-Saldaña, A.M. Alsharabasy, M.D. Costa, L. Feng, Z. Zhang, X. Ge, C. Li, S. Lu, A. Pandit, Plant-inspired multifunctional bioadhesives with self-healing adhesion strength to promote wound healing, Adv. Mater. Interfac. (2022), 2201599, https://doi.org/10.1002/admi.202201599.

[50] W.S. Kim, B.S. Park, H.K. Kim, J.S. Park, K.J. Kim, J.S. Choi, S.J. Chung, D.D. Kim, J.H. Sung, Evidence supporting antioxidant action of adipose-derived stem cells: protection of human dermal fibroblasts from oxidative stress, J. Dermatol. Sci. 49 (2008) 133–142, https://doi.org/10.1016/j.jdermsci.2007.08.004.

[51] R. Masaeli, K. Zandsalimi, L. Tayebi, Biomaterials evaluation: conceptual refinements and practical reforms, Ther. Innov. Regul. Sci. 53 (2019) 120–127, https://doi.org/10.1177/2168479018774320.

[52] K. Torres, L. Pietrzyk, Z. Plewa, K. Zaluska-Patel, M. Majewski, E. Radzikowska, A. Torres, TGF-beta and inflammatory blood markers in prediction of intraperitoneal adhesions, Adv. Med. Sci. 63 (2018) 220–223, https://doi.org/10.1016/j.advms.2017.11.006.

[53] Y. Kaneko, Y. Hirata, I. Achiwa, H. Morishita, H. Soto, J. Kobayahsi, Adhesion barrier reduces postoperative adhesions after cardiac surgery, Asian Cardiovasc. Thorac. Ann. 20 (2012) 257–262, https://doi.org/10.1177/0218492311435154.

[54] H. Sies, Hydrogen peroxide as a central redox signaling molecule in physiological oxidative stress: oxidative eustress, Redox Biol. 11 (2017) 613–619, https://doi.org/10.1016/j.redox.2016.12.035.

[55] A. Abudukeyoumu, M. Li, F. Xie, Transforming growth factor-β1 in intrauterine adhesion, Am. J. Reprod. Immunol. 84 (2020), e13262, https://doi.org/10.1111/aji.13262.

[56] R.K. Leung, Y. Lin, Y. Liu, Recent advances in understandings towards pathogenesis and treatment for intrauterine adhesion and disruptive insights from single-cell analysis, Reprod. Sci. 28 (2020) 1812–1826, https://doi.org/10.1007/s43032-020-00343-y.

[57] J. Chen, X. Yi, P. Gu, S. Gao, The role of KDR in intrauterine adhesions may involve the TGF-β1/Smads signaling pathway, Braz. J. Med. Biol. Res. 52 (2019), e8324, https://doi.org/10.1590/1414-431x20198324.